Nucleation and Island Growth of Alkanethiolate Ligand Domains on Gold Nanoparticles

Yifeng Wang,[†] Offer Zeiri,[†] Alevtina Neyman,[†] Francesco Stellacci,[‡] and Ira A. Weinstock[†,*]

[†]Department of Chemistry and the Ilse Katz Institute for Nanoscale Science and Technology, Ben Gurion University of the Negev, Beer Sheva, 84105, Israel and [‡]Institute of Materials, École Polytechnique Fédérale de Lausanne (EPFL), Lausanne, Switzerland, and Department of Materials Science and Engineering, Massachusetts Institute of Technology, Cambridge, Massachusetts 02139, United States

ABSTRACT The metal oxide cluster α-$AlW_{11}O_{39}^{9-}$ (1), readily imaged by cryogenic transmission electron microscopy (cryo-TEM), is used as a diagnostic protecting anion to investigate the self-assembly of alkanethiolate monolayers on electrostatically stabilized gold nanoparticles in water. Monolayers of 1 on 13.8 ± 0.9 nm diameter gold nanoparticles are displaced from the gold surface by mercaptoundecacarboxylate, $HS(CH_2)_{10}CO_2^-$ (11-MU). During this process, no aggregation is observed by UV—vis spectroscopy, and the intermediate ligand-shell organizations of 1 in cryo-TEM images indicate the presence of growing hydrophobic domains, or "islands", of alkanethiolates. UV—vis spectroscopic "titrations", based on changes in the surface plasmon resonance upon exchange of 1 by thiol, reveal that the 330 ± 30 molecules of 1 initially present on each gold nanoparticle are eventually replaced by 2800 ± 30 molecules of 11-MU. UV—vis kinetic data for 11-MU-monolayer formation reveal a slow phase, followed by rapid self-assembly. The Johnson, Mehl, Avrami, and Kolmogorov model gives an Avrami parameter of 2.9, indicating continuous nucleation and two-dimensional island growth. During nucleation, incoming 11-MU ligands irreversibly displace 1 from the Au-NP surface *via* an associative mechanism, with $k_{nucleation} = (6.1 \pm 0.4) \times 10^2\ M^{-1}\ s^{-1}$, and 19 ± 8 nuclei, each comprised of *ca.* 8 alkanethiolates, appear on the gold-nanoparticle surface before rapid growth becomes kinetically dominant. Island growth is also first-order in [11-MU], and its larger rate constant, k_{growth}, $(2.3 \pm 0.2) \times 10^4\ M^{-1}\ s^{-1}$, is consistent with destabilization of molecules of 1 at the boundaries between the hydrophobic (alkanethiolate) and the electrostatically stabilized (inorganic) domains.

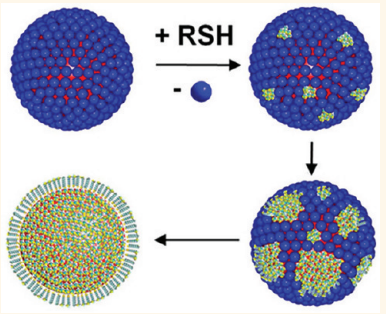

KEYWORDS: alkanethiol · monolayer · gold nanoparticle · island growth · cryo-TEM · kinetics

Over the past two decades, numerous studies have documented the nucleation and growth of "island"-like ligand-shell domains during the self-assembly of alkanethiolate monolayers on planar gold surfaces.[1] The first direct images of these nanoscale domains were obtained by scanning tunneling microscopy (STM) after the exposure of planar Au(111) to alkanethiols[2] under ultrahigh vacuum.[3] For the more common solution deposition[4] of alkanethiols, STM,[5] atomic force microscopy (AFM),[6,7] and kinetic data from numerous macroscopic methods[4] show that monolayer self-assembly[8] involves two distinct phases: nuclei formation, followed by two-dimensional growth of island domains.

Much less is known about alkanethiolate self-assembly on gold nanoparticles in solution.[1,9,10] Notably, direct measurements of self-assembled monolayer formation kinetics on gold nanoparticles are "rarely seen in the literature".[11] For gold nanoparticles with completed ligand shells, high-quality studies address alkanethiolate coordination,[12] the physical properties of neutral[13] and charged ligand shells,[1,12,14] and the kinetics of ligand "place exchange".[9,15] At the same time, gold nanoparticles with ligand shells tailored for applications[14,16] in biomedicine,[17,18] as sensors,[19] in catalysis,[12,20–23] and as building blocks for nanoparticle-based assemblies[24–27] are frequently prepared by reacting functionalized alkanethiols with electrostatically stabilized gold nanoparticles.[10,19,24,28–30] However, due to the difficulty of obtaining direct images[31–33] of intermediate ligand-shell structures and problems associated with particle aggregation in solution,[34] little is known about the mechanism(s) and intermediate ligand-shell structures involved in the self-assembly of alkanethiolate monolayers on colloidal gold nanoparticles. Yet, it is these intermediate ligand-shell structures that determine the particles' tendency toward aggregation and, hence, the reproducibility of this important class of "place-exchange" reactions.

Recently, cryogenic "trapping" was used in conjunction with transmission electron microscopy (*i.e.*, cryo-TEM) to obtain the first direct images of self-assembled monolayers

* Address correspondence to iraw@bgu.ac.il.

Received for review October 23, 2011 and accepted December 4, 2011.

Published online December 05, 2011
10.1021/nn204078w

of inorganic anions on electrostatically stabilized silver[35] and gold[36] nanoparticles in water. The inorganic ligands are metal-oxide cluster anions[37−39] or polyoxometalates (POMs; *e.g.*, α-$X^{n+}W_{12}O_{40}^{(8-n)-}$, $X^{n+} = Al^{3+}$ or "$2H^{+}$", and α-$X^{n+}W_{11}O_{39}^{(12-n)-}$, $X^{n+} = P^{5+}$, Si^{4+}, or Al^{3+})[40−42] that possess large negative charges for association with the gold surface, and W atoms ($Z = 74$) for TEM imaging. We now use the undecatungstoaluminate anion, α-$AlW_{11}O_{39}^{9-}$ (**1**, $X^{n+} = Al^{3+}$),[40−42] as a diagnostic stabilizing ligand for investigating the self-assembly of alkanethiolate ligand shells on a gold nanoparticle (Figure 1).

First, ligand exchange is used to assemble monolayers of **1** (Figure 1, bottom center) on the surfaces of 13.8 ± 0.9 nm gold nanoparticles (Figure 1, B).[36] During alkanethiolate-monolayer formation, molecules of **1** are then displaced by mercaptocarboxylates such as 3-mercaptoproprionate (**3-MP**), 11-mercaptoundecanoate (**11-MU**) (Figure 1, right), and 16-mercaptohexadecanoate (**16-MH**), and the nanoscale domains resulting from this hydrophobic "etching" of the inorganic monolayer are revealed in cryo-TEM images. Because replacement of the inorganic (tungsten-oxide) by organic (alkanethiolate) ligands results in substantial decreases in the SPR absorbance, cryo-TEM images can be correlated with kinetic data obtained from time-dependent changes in the UV−vis spectra.

This combined use of cryo-TEM imaging and UV−vis spectroscopy, both facilitated by use of the metal-oxide cluster-anion ligand, **1**, provides unique access to remarkably detailed structural and mechanistic information, leading to a model that—for the first time—describes the nucleation and growth of hydrophobic nanodomains involved in the self-assembly of alkanethiolate monolayers on the surfaces of electrostatically stabilized gold nanoparticles.

RESULTS AND DISCUSSION

Correlating cryo-TEM Imaging with UV−Vis Spectroscopy. Cryo-TEM imaging was combined with UV−vis spectra of the surface plasmon resonance (SPR) to reveal the ligand-shell domains and growth mechanism(s) associated with the formation of alkanethiolate monolayers on electrostatically stabilized gold nanoparticles (Au NPs). This approach is demonstrated in Figure 2.

As aliquots of sodium 11-mercaptoundecanoate (**11-MU**, 500 μM stock solution) are added to a solution of α-$AlW_{11}O_{39}^{9-}$ (**1**)-protected Au NPs (Figure 2, A and B), the SPR absorbance maximum decreases from 1.00 to 0.84 and is blue-shifted slightly from 526 to 520 nm (Figure 2, C and D). The change in SPR absorbance is due to the displacement of **1** and the large difference in refractive index between the metal-oxide cluster anions and the organic thiols. Hence, once all the inorganic ligands, **1**, have been displaced by the alkanethiolate, no further changes in the UV−vis spectra are observed.

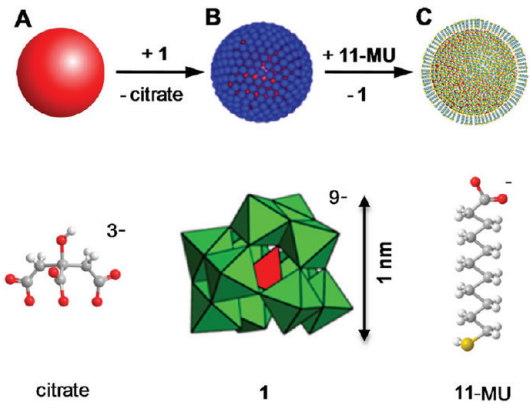

Figure 1. Use of metal-oxide cluster anions as "reporter" ligands for cryo-TEM imaging and UV−visible spectroscopic analysis of alkanethiolate-monolayer self-assembly. The structures of the three anionic ligands at the bottom of the figure are drawn to the same scale. Citrate-stabilized 13.8 ± 0.9 nm diameter gold nanoparticles (A; the citrate anion is shown below) are reacted with α-$K_9AlW_{11}O_{39}$ ($K_9$1) to give monolayers of the heteropolytungstate (B; molecules of 1 are shown in blue, with the counter-cations omitted for clarity). Bottom center: The cluster anion, 1, shown in polyhedral notation, includes 11 hexacoordinate W(VI) atoms (green polyhedra, with oxygen atoms at their vertices) encapsulating a tetrahedral-symmetry (formally) aluminate oxo-anion, $Al^{III}O_4^{5-}$ (red tetrahedron). During alkanethiolate-monolayer formation, molecules of 1 are displaced from the gold surface by mercaptocarboxylates, such as 11-mercaptoundecanoate (C, 11-MU, right). Resultant changes in the inorganic monolayer—revealed in cryo-TEM images—are used to locate the bound alkanethiolate ligands, and corresponding changes in the surface plasmon resonance (SPR) are quantified by UV−vis spectroscopy.

Relative to the W atoms in **1**, the alkanethiolate ligands are much less effective at scattering electrons and, therefore, are not seen in cryo-TEM images of the thiolate-protected NPs (Figure 2, E and F).

The UV−vis spectra in Figure 2D show the relatively large change in SPR absorbance associated with complete conversion of the inorganic monolayer of **1** (Figure 2A) to the organic ligand shell comprised of **11-MU** (Figure 2E). As a result, smaller changes in the SPR absorbance could be used to quantify degrees of surface coverage by molecules of **11-MU** *during* their self-assembly on the nanoparticle surface, while cryo-TEM was used in tandem to directly observe intermediate nanoscale ligand-shell domains. Once these intermediate structures were identified, stopped-flow kinetic methods were used to define the rates and mechanism(s) of the reactions associated with their formation and growth.

Quantitative Replacement of Inorganic Ligands by Alkanethiolates. A solution of Au NPs, stabilized by monolayers of **1** (Figure 2A), was titrated[29] with small aliquots of 500 μM solutions of **11-MU**, and UV−vis spectroscopy was used to quantify the gradual replacement of **1** by alkanethiolates on the Au NP surface. After adding each aliquot of **11-MU**, the intensity of the SPR absorbance maximum, initially at 526 nm, decreased rapidly to a new value (Figure 3A), and a slight blue-shift was

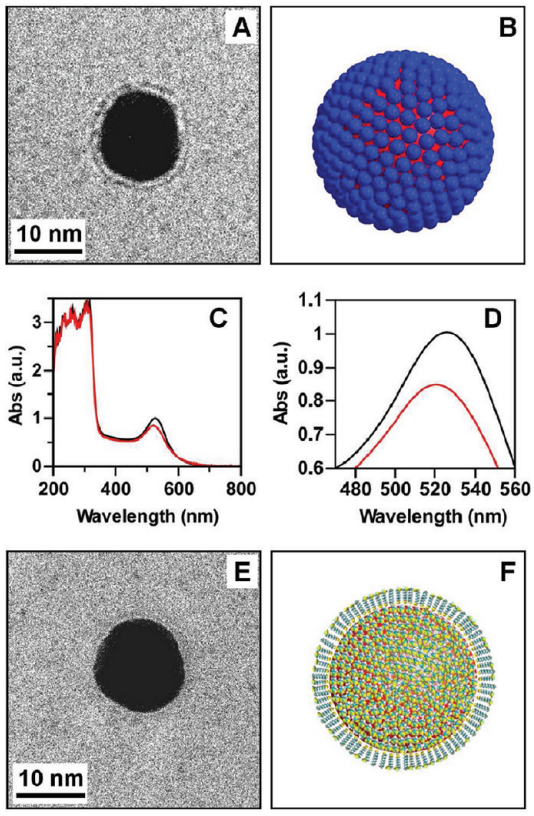

Figure 2. Replacement of inorganic stabilizing anions, 1, by 11-mercaptoundecanoate (11-MU). (A) Cryo-TEM image of a 1-protected Au NP. The illustration in panel B depicts a monolayer of 1 on the gold surface, as indicated by the two-dimensional-projection image in panel A. Panel C shows UV–vis spectra obtained before (black) and after (red) replacement of 1 by 11-MU, and an enlarged view of the region near the SPR absorbance maxima is given in panel D. Panel E is a cryo-TEM image of a Au NP after complete replacement of 1 by 11-MU, and space-filling models of the thiolate ligands (not observed by TEM) are illustrated in panel F. For simplicity, counter-cations are omitted from B and F.

noted, which rules out aggregation as the source of the decrease in absorbance. After providing time for completion of reaction (about 10 min; see Figure S1), the new absorbance value was recorded, and an additional aliquot was added. A plot of each new absorbance value as a function of the total **11-MU** concentration revealed a linear relationship (Figure 3B; $R^2 > 0.998$). Because changes in the SPR result from the displacement of **1** from the Au surface, this linear relationship argues against the alkanethiolates initially "lying down" on the gold-nanoparticle surface (see SI for more discussion). After the total concentration of **11-MU** reached 8.7 μM, further additions of **11-MU** did not cause significant changes in absorbance. This "break point" (at 8.7 μM), therefore, indicates the alkanethiol concentration at which all the molecules of **1** have been displaced from the Au-NP surface (see Figure 2, E).

Titration plots were obtained for two additional mercaptocarboxylates, 3-mercaptopropionate ($HS(CH_2)_2CO_2^-$, **3-MP**) and 16-mercaptohexadecanoate

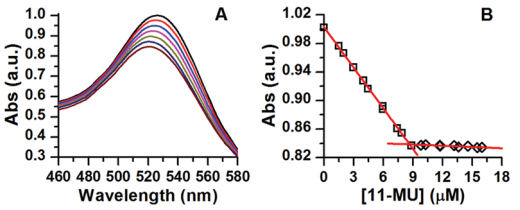

Figure 3. UV–vis profiles of Au NPs during displacement of 1 by 11-MU. (A) SPR absorbance spectra of the Au-NP solution after incremental additions of 11-MU. Absorbance maxima decreased after each addition, and spectra were recorded after equilibration (*ca.* 10 min). (B) Absorbance values at 526 nm as a function of total 11-MU concentration.

($HS(CH_2)_{10}CO_2^-$, **16-MH**) (see Figures S2 and S3). For all three mercaptocarboxylates, the plots are linear before and after the breakpoints, which occur at similar alkanethiol concentrations (see Table S1).

Meanwhile, the linear relationship in Figure 3B indicates that the binding constant for association of **11-MU** with the Au-NP surface, $K_{11\text{-MU}}$, should be *at least* 6 orders of magnitude larger than that for **1**, K_1 (this is shown in Figures S4–S6 in the Supporting Information). The ratio of K_1[36] to the binding constant for citrate, *i.e.*, $K_1/K_{citrate}$, is ca. 27,[43] such that $K_{11\text{-MU}}/K_{citrate} \geq 10^7$, a reasonable value given the large (>14.0 kcal·mol^{-1}) energies[44,45] estimated for the adsorption of alkanethiolates to the surfaces of gold nanoparticles. More significantly, the magnitude of $K_{11\text{-MU}}$ indicates that at **11-MU** concentrations less than or equal to the breakpoint in Figure 3B at least 99.9% of the **11-MU** ligands are bound to the Au NPs. Hence, *the average number of molecules of 11-MU present on the surface of each 13.8 ± 0.9 nm Au NP at the breakpoint is known with remarkable precision.* This makes it possible to calculate the average number of ligands on each Au NP after complete replacement of **1** by **11-MU**. (Because some additional thiol may add to the Au-NP surface after the breakpoint, the 8.7 μM value in Figure 3 provides a lower limit for the number of thiols on each Au NP upon complete displacement of the POMs.)

From the total concentration of Au(0) (0.25 mM) and the average diameter of the Au cores (13.8 nm), the concentration of Au NPs is 3.1×10^{-9} M. The average number of **11-MU** molecules on the surface of each Au NP at the breakpoint (8.7 μM) is given by the ratio of their concentrations: [**11-MU**]/[Au NP], or 2.8×10^3 molecules of **11-MU** per Au NP. This gives a molar surface density of 7.8×10^{-10} mol cm^{-2}. By dividing the surface area of the approximately spherical Au NPs ($4\pi r^2$, with the radius, r, in Å) by the number of **11-MU** molecules on each particle, one obtains a value of 21.3 Å^2 for the "footprint" of each **11-MU** molecule.

Each **1**-protected 13.8 nm diameter Au NP contains a ligand shell of 330 ± 30 molecules of **1**, whose "footprint" is therefore 181 ± 16 Å^2.[36] Hence, the alkanethiolate footprint of 21.3 Å^2 indicates that each

molecule of **1** is replaced by *ca*. 8.5 equivalents of **11-MU**. In addition, the footprint of **11-MU** is close to three times the 7.2 Å^2 area[46] occupied by a single Au atom on the nanoparticle's largely Au(111) surface, suggesting that, on average, each alkanethiolate is bound to three Au atoms. This is consistent with the $\sqrt{3}\times\sqrt{3}R30°$ structure established for bonding of alkanethiolates to planar Au(111) surfaces,[1] while not excluding other bonding arrangements that may give a similar average footprint, such as the RS-Au-RS-Au-RS "staple" motifs found in X-ray crystal structures of nanometer-sized gold clusters,[47,48] as well as on flat surfaces.[49] The relatively small footprint of the alkanethiolate also requires that its alkane chain and end group extend outward from, rather than lie down on, the Au-NP surface.

More generally, the "footprints" of alkanethiolates on gold surfaces vary with the structures and properties of the ligand and with the shape and size of the metal surface. For example, reported footprints for *n*-octanethiolates on small Au NPs in organic solvents range from 13 to 14 to 16 Å^2, on 1.5,[50] 2.4,[51] and 5.2 nm NPs,[50,52] respectively, while a footprint of 21.4 Å^2 has been reported on planar Au(111). For alkanethiols with polar end groups, however, *e.g.*, 6-mercaptopurine (6MP) on small, $Au_{459}(6MP)_{62}$, nanoparticles in water, a footprint of 29 Å^2 is obtained.[53] Hence, the 21.3 Å^2 value obtained for **11-MU** is consistent with both the polar nature of this alkanethiolate ligand and the size and less acute surface curvature of the 13.8 nm Au NPs used in the present work.

Alkanethiolate "Island" Domains on Gold Nanoparticles. Precise numbers of mercaptocarboxylate ligands were assembled on the surfaces of the Au NPs by adding ligand concentrations associated with specific degrees of displacement of **1** (see Figure 3B and Table S1). For this, solutions of **11-MU** (as Na^+ salts in water) were added with vigorous stirring to **1**-protected Au-NP solutions, after which the homogeneous solutions were stored for 24 h at room temperature. Cryo-TEM was then used to observe the corresponding inorganic-anion domains.

Final **11-MU** concentrations corresponding to 20%, 50%, and 70% displacements of **1** gave the cryo-TEM images shown in Figure 4. (See Figure 2E for an image obtained after 100% displacement of **1**.)

The POM ligand (**1**) contains W atoms (Z = 74), which provide better amplitude contrast than do alkanethiols. At the same time, the POMs are relatively small (*ca*. 1 nm in diameter) and are present as a dilute (thin) shell on the Au NPs, such that the very large amplitude contrast arising form the Au cores makes it difficult to use this contrast mechanism to image the POMs on their surfaces. To observe the POM ligands, "phase" contrast is used. For this, "under focus" is applied to the objective lens of the microscope. This adds additional phase shift to the transmitted electrons, providing additional contrast for imaging. An inherent

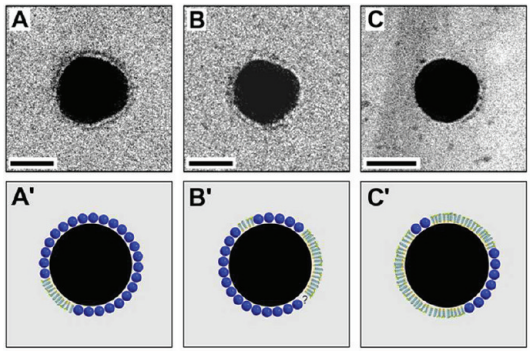

Figure 4. Cryo-TEM images obtained after adding mercaptoundecanoate (11-MU) to 1-protected gold nanoparticles. The images in panels A−C were obtained after titrating to 20%, 50%, and 70% surface coverage, respectively, by 11-MU. Panels A′−C′ illustrate the peripheral inorganic and organic ligand-domain organizations. The bar is 10 nm in length. Additional cryo-TEM images are provided as Supporting Information; see Figures S7−S12.

consequence of using "under focus" is the presence of thin "white" regions at the perimeters of the more electron dense Au cores. This can sometimes be minimized by repeated image acquisition using slightly different degrees of phase contrast. (An example of this is provided in Figure S7 in the Supporting Information.) Overall, if the objects of interest are clearly discernible, definitive information regarding the presence and relative locations of the smaller (1−2 nm), less electron dense objects can be obtained despite the presence of the white regions inherent in the use of phase contrast.

Compared with the complete "rings" of cluster anions in cryo-TEM images of **1**-protected Au NPs (*cf*. Figure 2A), discrete "strand"-like regions of **1** are now observed around the perimeter of the Au core. The majority of the cluster anions, **1**—located on the superior and anterior hemispheres of the Au NPs—are obscured by the Au atoms and are not seen in the cryo-TEM images. Nevertheless, the intact "strands" of **1** observed at the peripheries of the Au cores are indicative of "island"-like domains of the inorganic ligand on the nanoparticle surface. The peripheral regions that no longer contain molecules of **1** are now occupied by the alkanethiolate ligands, as illustrated in panels A′−C′, and these regions are similarly indicative of complementary "island" domains of the organic ligands on the particle surface. For 70% surface coverage by **11-MU**, for example (panel C), the inorganic domains of **1** occupy *ca*. 30% of the gold-core circumference. While the precise numbers of molecules of **1** in the peripheries of each gold core depend on orientation of the particle relative to the electron beam, a definitive trend is observed, as shown in the representative images selected for inclusion in Figure 4. Similar results were obtained for **3-MP** and **16-MH** (see Figures S13 and S14, Supporting Information). Consistent with these findings, phase-separated nanodomains

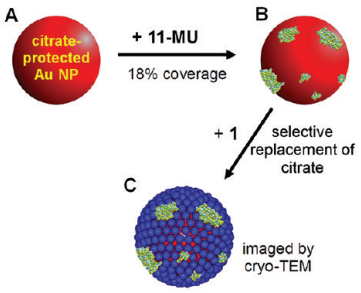

Scheme 1. Use of α-$AlW_{11}O_{39}^{9-}$ (1) to reveal alkanethiolate domains on citrate-stabilized gold nanoparticles.

were recently observed by FTIR spectroscopy after alkanethiols (including mercaptoundecanoic acid)[54] were added to Au NPs stabilized by diphenylphosphinnine (phosphinnine being the phosphorus analogue of pyridine).[55] While the ligand organizations in the cryo-TEM images in Figure 4 are limited to two dimensions, they clearly demonstrate the formation of separate "island" domains. *This makes it possible to definitively interpret UV–vis kinetic data associated with alkanethiolate-monolayer formation (below), so as to provide a quantitative picture of nucleation and island growth.*

Meanwhile, to assess the stabilities of the organic-ligand island domains, an amount of **11-MU** designed to give 37% alkanethiolate coverage was added to a solution of **1**-protected Au NPs, and the resultant solution was heated to 80 °C for 4 h. These conditions are sufficient to equilibrate adsorption/desorption of the inorganic ligands, **1** (see data in refs 36 and 43). Cryo-TEM sampling was performed immediately after cooling to room temperature. The resultant images (Supporting Information, Figure S15) revealed island domains that, with respect to their general features, were similar to those observed in unheated samples. Hence, the "island" domains in Figure 4 possess substantial kinetic stabilities relative to perfectly mixed or, alternatively, to Janus-like arrangements of the two ligand types.[56]

Similar island domains are likely formed when alkanethiols are reacted with Au NPs electrostatically stabilized by other, more typical, protecting ions. Direct evidence for this was provided using the procedure summarized in Scheme 1, in which citrate serves as a typical anionic ligand.

First, **11-MU** was reacted with citrate-protected Au NPs (A in Scheme 1), for which $K_{\mathbf{11}\text{-MU}}/K_{\text{citrate}} \geq 10^7$. Based on the titration curve in Figure 3B, the amount of **11-MU** used was designed to give 18% coverage by the alkanethiolate (B in Scheme 1; the thiolates are shown in green). After 5 h, citrate ligands remaining on the gold surface were replaced by **1** ($K_{\mathbf{1}}/K_{\text{citrate}} = 27$),[43] to give C (molecules of **1** are shown in blue). For this, an excess of K_9**1** was added, the solution was stored at room temperature for 18 h, and cryo-TEM samples were then prepared. The resultant mixed ligand-shell

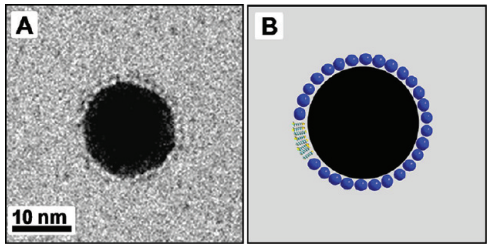

Figure 5. Alkanethiolate "island" domains on citrate-stabilized Au NPs. Citrate-stabilized Au NPs were reacted with 11-MU (18% calculated coverage) followed by the addition of 1 as shown in Scheme 1. Cryo-TEM samples were prepared after 18 h. (A) Representative cryo-TEM image; (B) illustration showing the incomplete peripheral "necklace" of 1. See Figure S16 for additional images.

structures, with **1** in the regions *previously occupied by citrate*, were then imaged by cryo-TEM (Figure 5).

The incomplete peripheral "necklace" of **1**, illustrated for clarity in Figure 5B, is consistent with island domains of **11-MU** in the mixed alkanethiolate/*citrate* ligand shell of particle B in Scheme 1 (see Supporting Information, Figure S16, for images featuring multiple "island" domains). This suggests that similar island domains may be present in the mixed-ligand shells of numerous functional gold nanoparticles prepared by reacting biologically or chemically active thiol derivatives with electrostatically stabilized Au NPs in water.[10,19,24,28–30,55]

Kinetics of Alkanethiolate-Monolayer Formation. The large change in SPR absorption intensity that accompanies replacement of **1** by **11-MU** (Figures 2 and 3) was used to investigate the kinetics of alkanethiolate-monolayer self-assembly. For this, solutions of **11-MU** were reacted with **1**-protected 13.8 ± 0.9 nm diameter Au NPs using a stopped-flow apparatus for rapid mixing.

To assess the dependence of monolayer-growth rates on [**1**] and [**11-MU**], each was varied while keeping the other constant (Figure 6). Specifically, final concentrations of **1** were varied from 1.0 to 4.0 mM at 8.0 μM **11-MU** (panel A), and final concentrations of [**11-MU**] were varied from 4.0 to 16.0 μM at [**1**] = 1.0 mM (panel B). For both sets of experiments, the absorbance *versus* time curves displayed sigmoidal profiles indicative of two kinetically distinct processes: a slow initial phase, followed by a rapid-growth phase.

When [**1**] was varied at constant [**11-MU**] (panel A), the kinetic traces were superimposable within experimental uncertainty. The reaction is thus zero-order in [**1**], ruling out a rate-limiting pre-equilibrium involving reversible dissociation of **1** from the Au-NP surfaces. However, when [**11-MU**] was varied (at constant [**1**]), a series of different curves was obtained (panel B).

Because island domains were revealed in cryo-TEM images (Figure 4), the sigmoidal curves in Figure 6 were evaluated using the JMAK model for nucleation and growth.[57] Originally derived for phase transitions in metal alloys, this model was recently used by Weiss[57]

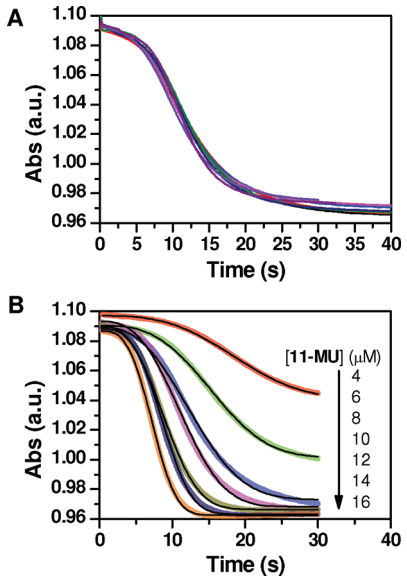

Figure 6. Stopped-flow UV–vis spectral traces of SPR absorbance values (at 526 nm) upon reactions of 11-MU with 1-protected Au NPs. (A) Effectively identical traces obtained as final concentrations of 1 were varied (in 0.5 mM increments) from 1.0 to 4.0 mM at (constant) 8.0 μM 11-MU. (B) Traces corresponding to final 11-MU concentrations at (constant) 1.0 mM 1. The black curves in B are fits to the Johnson, Mehl, Avrami, and Kolmogorov (JMAK) model (see text).

to describe the displacement of 1-adamantanethiolate monolayers from planar gold surfaces. To apply the JMAK model, the traces in Figure 6B were written in terms of the time-dependent absorbance, $A(t)$, as shown in eq 1. Here A_1 and A_2 are the initial and final absorbance values, respectively, k_{JMAK} is an apparent rate constant, and n is an adjustable exponent, referred to as the "Avrami" parameter (see Supporting Information for more details).

$$A(t) = A_2 + (A_1 - A_2)\exp[-(k_{JMAK}t)^n] \quad (1)$$

When kinetic data for the nucleation and growth of two-dimensional films are fitted to eq 1, the Avrami parameter varies from $n = 2$ for cases in which saturation of nucleation sites occurs early in the reaction, to $n = 3$ for cases in which nucleation rates remain constant throughout film formation.[58] Using eq 1, excellent fits to the kinetic traces were obtained (black curves in Figure 6B), and an Avrami parameter of $n = 2.9 \pm 0.3$ indicated a two-dimensional continuous-nucleation and island-growth mechanism (see Figures S17 and S18).[57–59]

The constant, k_{JMAK}, in eq 1 can be treated as an apparent rate constant.[57] When the k_{JMAK} values from fits to the curves in Figure 6B were plotted as a function of [**11-MU**], a linear relationship was obtained (Figure 7).

This first-order dependence on [**11-MU**] indicates that monolayer formation occurs *via* associative displacement of **1** by incoming molecules of **11-MU**. Importantly, this associative mechanism is consistent with the "continuous-nucleation" process indicated by

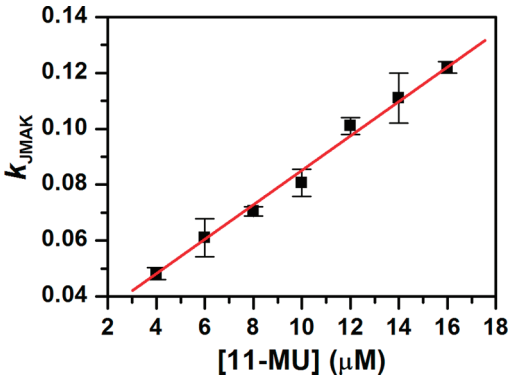

Figure 7. Rate constants, k_{JMAK}, from the JMAK model for nucleation and island growth, eq 1, as a function of [11-MU]. Uncertainties (error bars) were determined by repeated measurements.

the Avrami parameter of $n = 2.9 \pm 0.3$. For the exchange of 1-adamantanethiolate by *n*-dodecanethiolate on planar-gold surfaces, Weiss[57] found an Avrami parameter of $n = 2$, and rather than the expected first-order dependence of k_{JMAK} on [*n*-dodecanethiol], an unambigously half-order dependence was observed.

The JMAK model applies here (*i.e.*, in Figures 6 and 7) because two criteria are met. First, the ligand exchange is slow enough to permit kinetic resolution of the nucleation phase of the reaction. Second, the surface area of each 14 nm Au NP particle is large enough (330 POM ions replaced by at least 2800 thiolates) for multiple nucleation sites to occur during the more rapid "island" growth. However, the excellent fit to the JMAK model observed in Figure 6 may not be obtained if the nucleation phase is too rapid or if the surface area of the particle is too small. This was noted in the present work when the JMAK model was applied to the displacement of **1** from smaller (6 nm) Au NPs. There, reasonable fits were obtained, but the Avrami parameter was *ca.* 1.2, smaller than the range of 2–3 allowed for by the model (see Table S3). It thus appears that the nucleation rate and total surface area are more significant with respect to application of the JMAK model than are the relative footprints of the incoming and displaced ligands. For the common situation in which relatively weakly bound citrate ligands are displaced from 3 to 5 nm core nanoparticles, nucleation should be more rapid than for displacement of **1**, and the surface area is relatively small. In those cases, although "island growth" during place-exchange is suggested by cryo-TEM (Figure 5), an analytical approach to the kinetic data, involving independent measurements of the nucleation and growth rates (as shown immediately below), is likely to prove more informative.

The sigmoidal curves in Figure 6 arise from a substantial difference in rates between (slow) nucleation and (more rapid) growth processes. Each of these kinetically distinct regions is now analyzed in more detail using data from cryo-TEM and UV–vis spectroscopy that reveal how the numbers of each ligand

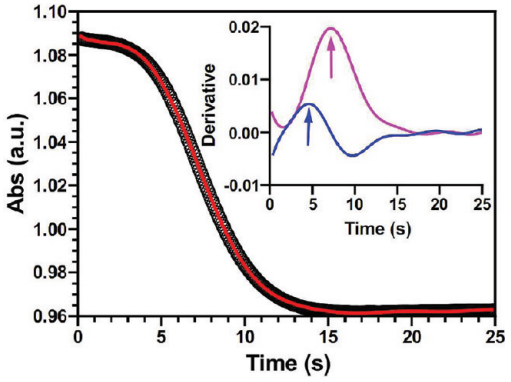

Figure 8. Kinetic analysis of 11-MU-monolayer formation on colloidal gold nanoparticles. The representative absorbance *versus* time curve in the figure was obtained using 16 μM 11-MU and 1.0 mM 1. The experimentally measured curve (black) was smoothed using the function $y = \sum_{n=0}^{n=15} a_n x^n$ (red curve, R^2 = 1.0000). The "maximum" in the first derivative of this function (the pink curve in the inset, with units of au s^{-1}) is the maximum rate achieved during the rapid phase, while the "maximum" in its second derivative (the blue curve in the inset) was used to identify the end of the slow phase.

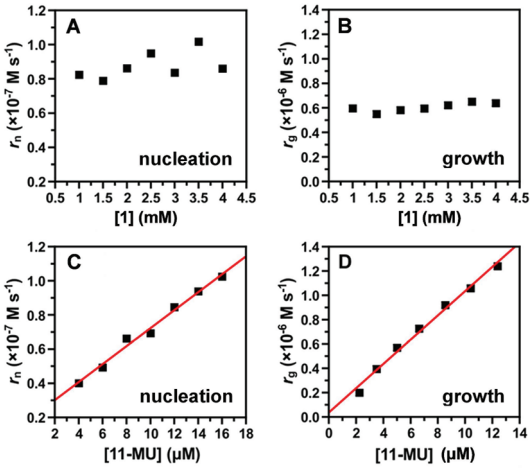

Figure 9. Nucleation and island-growth rates as functions of [1] and [11-MU]. Nucleation and maximum island-growth rates are zero-order in [1] (panels A and B, respectively) and first order in [11-MU] (panels C and D). The uncertainty in reported values is ±14% and was estimated from statistical analysis of repeated measurements.

(**1** and **11-MU**) vary with time on the Au-NP surface, leading to a detailed model for self-assembly of the alkanethiolate monolayer.

Nucleation and island-growth rates were determined using the method demonstrated in Figure 8 (see caption for details). The method and results are discussed below, first for nucleation and then for island growth.

Nucleation. The duration of each slow phase was obtained as the maximum in the second derivative of each absorbance *versus* time trace (blue curve and arrow in the inset to Figure 8). (This is referred to below as the "nucleation" phase, recognizing that it actually represents the nucleation that occurs *before* rapid growth becomes kinetically dominant.) The average rates associated with the nucleation phase, in units of au s^{-1}, were obtained by dividing changes in SPR absorbance by the corresponding nucleation times. Molar rates, *i.e.*, in units of M^{-1} s^{-1}, were calculated using data from the UV−vis titration curve for the displacement of **1** by **11-MU**. From the breakpoint in Figure 3B, the change in the SPR absorbance for complete replacement of all molecules of **1** by **11-MU** is 0.13 ± 0.01 au. This corresponds to an 8.7 μM concentration of adsorbed **11-MU**, giving a conversion factor of 1 au per 6.69×10^{-5} M **11-MU**. This conversion factor was used to obtain molar rates for the nucleation phase, which are plotted in Figure 9 as respective functions of [**1**] (panel A) and [**11-MU**] (panel C).

Consistent with the data in Figure 6A, the rate is invariant as [**1**] is increased from 1.0 to 4.0 mM (panel A). Increase in [**11-MU**], however, results in a linear increase in rate, revealing a first-order dependence on [**11-MU**] (Figure 9C). Linear fitting (R^2 = 0.988) gives an apparent rate constant of $k_{app} = (5.3 \pm 0.3) \times 10^{-3}$ s^{-1}. Dividing k_{app} by the concentration of available alkanethiolate binding sites (8.7×10^{-6} M, the concentration of **11-MU** associated with the breakpoint in Figure 3B) gives a second-order rate constant for the nucleation phase of $k_{nucleation} = (6.1 \pm 0.4) \times 10^2$ M^{-1} s^{-1}. These data are consistent with an associative mechanism for the nucleation of **11-MU** on the Au-NP surface. The rate constant for nucleation is relatively modest, consistent with the (net) negative charge of the electric double layer near the Au NPs,[36,43,60] which decreases the rate of diffusion of the negatively charged mercaptocarboxylates to the gold surface, in combination with a kinetic barrier to associative displacement of **1** from the NP surface.

For ligand place-exchange of 6-mercapto-1-hexanol thiol on 1.6 nm hexanethiolate-capped Au NPs, Murray has demonstrated that exchange initially occurs (to *ca.* 10%) at the edge and vertex sites.[61] This does not seem to be the case in the present study. If it were, nucleation would likely result in rapid site saturation. Rather, the kinetic stability of the anion-ligand monolayer[36] appears to be more important. This kinetic stability, consistent with the first-order dependence on [**11-MU**], is likely responsible for the continuous nucleation mechanism indicated by the JMAK model analysis. In addition, the kinetic data indicate that monolayer growth occurs at a time scale significantly shorter than that associated with alkanethiolate migration on the gold surface.

Island Growth. The first derivative of the absorbance *versus* time plot (pink curve and arrow in the inset to Figure 8) was used to determine the maximum island-growth rate in units of au s^{-1}. These values were converted to units of M s^{-1} as described above. The maximum rate is zero-order in [**1**] (Figure 9B), but first-order in [**11-MU**] (Figure 9D; see also Figure S19).

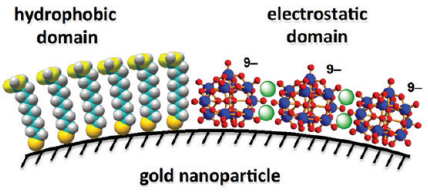

Figure 10. Interface between a hydrophobic "island" domain of 11-MU (space-filling models) and close-packed arrays of α-$AlW_{11}O_{39}^{9-}$ (1, in ball-and-stick notation). Green spheres in the inorganic domain are structurally integrated counter-cations and their hydration shells. For simplicity, the 11-MU molecules are drawn perpendicular to the surface. The rate constant, k_{growth}, for associative displacement of 1 at the domain boundaries—at which molecules of 1 are destabilized by proximity to the hydrophobic *n*-alkyl chains of 11-MU—is more than 35 times larger than the rate constant, $k_{nucleation}$, for displacement of cluster anions from *within* intact arrays of 1.

From the linear plot in panel D, the rate constant for island growth, k_{growth}, at its most rapid point (approximately 50% surface coverage) is $(2.3 \pm 0.2) \times 10^4$ M^{-1} s^{-1}, more than 35 times larger than that for nucleation, $k_{nucleation}$ (see calculations in the Supporting Information).

The larger rate constant for k_{growth} likely results from destabilization of **1** at the boundaries between the organic and inorganic domains. Despite their carboxylate end groups, the relatively long *n*-alkyl chains of the mercaptoundecanoate (**11-MU**) ligands form a largely hydrophobic domain. In contrast to this, the inorganic domains of **1** are stabilized by electrostatic interactions and by hydrogen bonding involving **1** and its hydrated counter-cations.[36,43,60] This difference plays an important role in formation of the "island" domains of **11-MU** observed in cryo-TEM images (Figures 4 and 5). At the same time, the physical properties of these two ligand types are likely responsible for the larger rate constant for k_{growth}. Nucleation, which is slower, involves the displacement of **1** from within *intact*, probably hexagonally packed, arrays of the cluster anion. During growth, however, molecules of **1** at the interfaces between the growing **11-MU** islands and the electrostatically stabilized arrays of inorganic cluster anions[36] are made more labile by proximity to the hydrophobic *n*-alkyl chains of the organic ligands (Figure 10). This should decrease the activation barrier to associative displacement of **1** by **11-MU** at the domain boundaries, rendering k_{growth} substantially larger than $k_{nucleation}$.

Self-Assembly of the Alkanethiolate Ligand Shell. The rate-constant ratio, $k_{growth}/k_{nucleation}$, is large enough to observe distinct nucleation and island-growth phases, yet not so large as to obscure the nucleation process by early onset of a kinetically dominant growth phase. Nevertheless, due to some contributions from island growth, the nucleation rate constant calculated above, *i.e.*, $k_{nucleation} = 6.1 \times 10^2$ M^{-1} s^{-1}, is probably somewhat larger than the actual value for nucleation alone. To assess this uncertainty, the percent changes in SPR

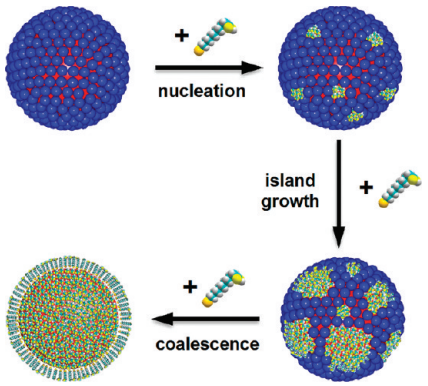

Scheme 2. Nucleation and growth of an alkanethiolate ligand shell on a 14 nm gold nanoparticle.

absorbance associated with the nucleation phases of the plots in Figure 6B were evaluated (see Supporting Information, Figure S20). The percent-change values were fairly constant, equaling 5.5 $\pm$ 2.2% of the total SPR change, ΔA, associated with the complete removal of **1** from the NP surface. Hence, a proportional uncertainty of 40% (*i.e.*, 2.2/5.5 $\times$ 100) must be assigned to the reported value for $k_{nucleation}$. More importantly, this percent-change value can be used to better understand the nucleation process itself.

From cryo-TEM images (*e.g.*, Figure 2A),[36,60] each **1**-protected 13.8 nm diameter Au NP contains a monolayer comprised of 330 molecules of **1** (top left in Scheme 2). On the basis of the data in Figure 3B and Table S1, these are replaced by 2800 molecules of **11-MU** (bottom left in Scheme 2). The 5.5 $\pm$ 2.2% absorbance change associated with nucleation thus corresponds to the binding of 150 $\pm$ 60 molecules of **11-MU** to each Au NP. In addition, the 2800/330 ratio indicates that each molecule of **1** is replaced by *ca.* 8 molecules of **11-MU**. Once a molecule of **1** is displaced from the Au-NP surface by a single equivalent of **11-MU** (consistent with the first-order dependence on [**11-MU**]), the exposed surface area is rapidly occupied by an additional 7 equivalents of the alkanethiolate. (The kinetic barrier to addition of these to the Au surface should be substantially smaller than that for the associative displacement of **1**.) Hence, each nucleus formed by associative displacement of a single molecule of **1** contains 8 molecules of **11-MU** (top right in Scheme 2), and 19 $\pm$ 8 of these nuclei appear before rapid island growth becomes kinetically dominant.

Once formed, the growth of these nuclei into "island" domains, and continued growth at their boundaries, is considerably more rapid. Nevertheless, the Avrami parameter of $n = 2.9$ indicates that nucleation *continues* during island growth. This is entirely consistent with—and in fact required by—the associative mechanism for nucleation indicated by the first-order dependence of nucleation rates on [**11-MU**] in Figures 7 and 9C. Namely, the associative displacement of **1** from *within* remaining inorganic domains of **1**

continues at the same (slow) rate during the more rapid growth of the organic domains (right in Scheme 2). At the same time, island growth, kinetically facilitated by the destabilizing influence of the growing hydrophobic domains on the electrostatically stabilized array of inorganic anions (Figure 10), results in rapid growth of the alkanethiolate ligand shell. Finally, rates decrease abruptly as the number of molecules of **1** available for displacement from the Au-NP surface decreases to a small value, and the alkanethiolate domains coalesce to give a complete monolayer (bottom of Scheme 2).

CONCLUSION

The metal oxide cluster anion α-$AlW_{11}O_{39}^{9-}$ (**1**), readily observed in cryo-TEM images, was used as a diagnostic protecting ligand for investigating the self-assembly of alkanethiolate monolayers on electrostatically stabilized gold nanoparticles in water. For this, monolayers of **1** on 13.8 ± 0.9 nm diameter gold nanoparticles were partially displaced from the gold surface by a series of mercaptocarboxylates, $HS(CH_2)_2CO_2^-$ (**3-MP**), $HS(CH_2)_{10}CO_2^-$ (**11-MU**), and $HS(CH_2)_{15}CO_2^-$ (**16-MH**). Cryo-TEM images of intermediate structures revealed localized regions of **1** that decreased in size as self-assembly of the alkanethiolate monolayer progressed. Hence, rather than intimate mixing of the two ligand types, the alkanethiolates formed nanoscale hydrophobic domains, or "islands", on the gold-nanoparticle surface. The generality of this phenomenon was suggested by the observation of similar island domains in cryo-TEM images obtained after using **1** to selectively displace citrate from the surfaces of nanoparticles protected by mixed, citrate/**11-MU**, ligand shells.

Quantitative information regarding monolayer formation was obtained by correlating cryo-TEM images with the decrease in the surface plasmon resonance absorbance that accompanied the replacement of **1** by **11-MU**. Notably, spectroscopic "titrations" revealed that the 330 ± 30 molecules of **1** initially present on each Au NP are eventually replaced by 2800 ± 30 molecules of **11-MU**. This information was then used to evaluate kinetic data obtained by stopped-flow measurements of changes in the SPR absorbance as a function of time during **11-MU**-monolayer formation.

The absorbance *versus* time curves revealed two distinct processes: a slow phase involving a small number of alkanethiolate ligands, followed by rapid self-assembly. The kinetic curves were first evaluated using the Johnson, Mehl, Avrami and Kolmogorov (JMAK) model for nucleation and growth. Weiss[57] recently applied this "universal" model to the place-exchange of alkanethiols on planar-gold surfaces, and data from the present study show it can provide insight into the two-dimensional growth of ligand shells on gold nanoparticles. The JMAK model gave good fits with an Avrami parameter of 2.9, indicative of a continuous-nucleation and island-growth mechanism.

Kinetic data for each phase were then evaluated using traditional solution-state methods, providing molar rate constants for nucleation and growth, and orders of reaction with respect to concentrations of **1** and **11-MU** during each of these processes. During nucleation, incoming mercaptocarboxylate ligands irreversibly displace **1** from the Au-NP surface *via* an associative mechanism, with a rate constant of $k_{nucleation}$ = (6.1 ± 0.4) × 10^2 M^{-1} s^{-1}. This associative mechanism is consistent with the continuous-nucleation model indicated by the Avrami parameter. Namely, nucleation—*via* displacements of **1** from inorganic domains—continues even as previously formed hydrophobic islands grow at the phase boundaries. Using the ligand-"titration" data noted above, it was found that 19 ± 8 nuclei, each comprised of *ca.* 8 alkanethiolates, form on the Au-NP surface before rapid growth becomes kinetically dominant. The larger rate constant for island growth (k_{growth} = (2.3 ± 0.2) × 10^4 M^{-1} s^{-1} at the rate maximum) likely arises from destabilization of molecules of **1** at the interfaces between the inorganic and growing alkanethiolate (hydrophobic) domains, leading to more rapid associative displacement of **1** at the phase boundaries. Finally, an abrupt decrease in rate is observed as the hydrophobic islands coalesce to give a complete monolayer.

These conclusions represent a detailed model that for the first time describes the self-assembly of alkanethiolate monolayers on a gold nanoparticle. This model, which includes the formation of discrete alkanethiolate nuclei by associative displacement of stabilizing ions from the gold surface, followed by the rapid growth of hydrophobic "island"-like domains, provides valuable insight into how tailored ligand shells might evolve during reactions of functional thiol-containing ligands with colloidal gold nanoparticles.

MATERIALS AND METHODS

Materials. α-$K_9AlW_{11}O_{39}$ (K_9**1**) was synthesized according to the literature method.[40−42] $HAuCl_4$ (99.9+%), trisodium citrate, $C_6H_5Na_3O_7 \cdot 2H_2O$ (analytical grade), 3-mercaptopropanoic acid ($HOOC(CH_2)_2SH$), 11-mercaptoundecanoic acid ($HOOC(CH_2)_{10}SH$), and 16-mercaptohexadecanoic acid ($HOOC(CH_2)_{15}SH$) were purchased from Sigma-Aldrich. For simplicity, the salt forms of the mercaptocarboxylic acids are abbreviated as **3-MP**, **11-MU**, and **16-MH**, respectively. All solutions were prepared using highly purified water (Millipore Direct-Q), added salts or buffers were of the highest purity available, and all glassware used for the synthesis and storage of gold-nanoparticle solutions was pretreated with fresh aqua regia (3:1 v/v ratio of HCl to HNO_3). All gold-nanoparticle solutions were stored at ambient temperature in the dark.

Instrumentation. UV−vis spectra were obtained using a Hewlett-Packard 8453 diode array spectrophotometer. Cryogenic sample preparation for transmission electron spectroscopy (cryo-TEM) was as previously described.[35,36] TEM and cryo-TEM

images were captured on a FEI Tecnai 12 G^2 instrument (120 kV) using a Gatan slow-scan camera. Kinetic data were obtained using an SX20 stopped-flow spectrometer (Applied Photophysics Ltd., UK) equipped with a photomultiplier. The reaction temperature was maintained by a JULABO F12-ED circulating bath at 24.3 ± 0.1 °C. The cell path length was 10 mm. Zeta potential data were obtained using a particle electrophoresis instrument (ZEM 3600, Zetasizer, Malvern Instruments Ltd.). Dynamic light scattering (DLS) data were collected at 25 °C on an ALV-CGS-8F instrument (ALV-GmbH, Germany).

Preparation of 1-Protected Gold Nanoparticles. Citrate-protected Au nanoparticles (Au NPs) were prepared by minor modification (published elsewhere)[36] of the Turkevich method.[62] The Au NPs were close to spherical and relatively monodisperse in size, with an average diameter of 13.8 ± 0.9 nm, based on TEM images (measurements of more than 100 particles)[36] and DLS data. Thus, for typical solutions containing 5.0×10^{-4} M Au (from $HAuCl_4$), the concentration of (on average) 13.8 nm Au NPs is 6.2×10^{-9} M. According to previous cryo-TEM analyses,[36] monolayers of **1** on each 13.8 nm Au NP are comprised (on average) of 330 ± 30 cluster anions. At effectively full surface coverage of the Au NPs, the concentration of bound anions, **1**, in 6.2×10^{-9} M solutions of the Au NPs is 2.0×10^{-6} M. To obtain this surface coverage, solutions of 4.0 mM K_9**1** were added to equal volumes of the citrate-protected Au NPs. The mixture was stored at 23 ± 2 °C in the dark for *ca.* 24 h to ensure complete formation of monolayers of **1**.[36] The pH values of citrate- and **1**-protected Au NPs were 6.0 and 7.2, respectively.

Reactions of 1-Protected Gold Nanoparticles with Alkanethiols. $HS(CH_2)_2CO_2H$ was dissolved in pure water, while for the less water-soluble thiols, $HS(CH_2)_{10}CO_2H$ and $HS(CH_2)_{15}CO_2H$, 2 and 4 equivalents, respectively, of NaOH were added to achieve complete dissolution by converting the mercaptocarboxylic acids to their salt forms, 11-mercaptoundecoate, $HS(CH_2)_{10}CO_2^-$ (**11-MU**), and 16-mercaptohexadecanoate, $HS(CH_2)_{15}CO_2^-$ (**16-MH**). Because the dissolved mercaptocarboxylates were oxidized slowly by ambient O_2, all solutions were prepared just prior to use. A UV–vis titration procedure, based on changes in SPR absorbance,[36] was used to quantify the replacement of **1** by thiolates on the surfaces of the Au NPs. For this, aliquots of the thiol-ligand solutions (5–10 μL of the 5.0×10^{-4} M solutions) were added sequentially to a spectrophotometer cell (path length = 1 cm) that contained 2 mL of the **1**-protected Au NPs. The temperature was maintained at 25.0 ± 0.1 °C.

Because final added mercaptocarboxylate concentrations were in the μM range, the added Na^+ (from neutralization of $HS(CH_2)_{10}CO_2H$ and $HS(CH_2)_{15}CO_2H$ by NaOH noted above) did not noticeably change the SPR spectra of the Au NPs. (Note: The pH values of the **1**-protected gold nanoparticle solutions were near neutral, and the small concentrations of added $HS(CH_2)_2CO_2H$ were effectively neutralized to $HS(CH_2)_2CO_2^-$ (**3-MP**) by the inherent buffering capacity of the *ca.* 4 mM concentrations of **1**. This same buffering capacity maintained the larger mercaptocarboxylates in their salt forms prior to reaction with the Au-NP surface.) After each aliquot was added, the system was allowed to equilibrate until the absorbance at 526 nm decreased to a plateau value (*ca.* 10 min). Because the SPR absorbance of the Au NPs was negligible at wavelengths > 750 nm, the absorbance at 780 nm was routinely subtracted from the final absorbance of 526 nm to eliminate small changes in baseline values upon additions of the thiols. Once the mercaptocarboxylates have become bound to the Au-NP surface, the pK_a values of the corresponding carboxylic acids can increase to values of 7 or greater.[63] Hence, the carboxylate groups of the *bound* alkanethiolates might be substantially protonated at the prevalent pH values of the Au-NP solutions (*i.e.*, at pH values between 6 and 7). Upon complete replacement of **1** by thiolates, zeta-potential values decreased from −62 mV (for the **1**-protected Au NPs)[36] to −42, −47, and −57 mV respectively for **3-MP**, **11-MU**, and **16-MH**.

Kinetic Stabilities of Alkanethiolate-Ligand Domains on 1-Protected Gold Nanoparticles. A solution of **1**-protected Au NPs was prepared as described above. On the basis of UV–vis titration data (see above), **11-MU** (3.2 μM after mixing) was added to achieve 37% coverage of the Au NPs by the thiolate ligand. Ligand exchange was completed within 10 min at room temperature (based on UV–vis spectroscopic analysis), after which the mixture was heated to 80 °C for 4 h. Immediately after cooling to room temperature, samples were prepared for cryo-TEM analysis.

Reactions of Alkanethiols with Citrate-Protected Gold Nanoparticles. Citrate-stabilized Au NPs were prepared as described above (0.5 mM in Au and an estimated NP concentration of 6.2×10^{-9} M). Then, **11-MU** was added to give a concentration of 3.2 μM. On the basis of data from titrations of **1**-protected Au NPs and the [Au] used here, this corresponded to 18% coverage by the thiolate. The mixture was kept at ambient temperature for 5 h, after which it was rapidly mixed with an equal volume of 4 mM K_9**1**. After 18 h at ambient temperature, samples were taken for cryo-TEM analysis.

Nucleation and Growth of Alkanethiolate Ligand Shells. Kinetic data were obtained at 24.3 ± 0.1 °C using a stopped-flow apparatus. The volume ratios of the Au NPs and alkanethiol solutions (prepared as described above) were 1:1. The absorbance change after mixing was followed at the initial absorbance maximum of the **1**-protected Au NPs, *i.e.*, 526 nm. UV–vis analysis[36] of changes in the SPR gives the fractional coverage of the Au NPs by **1** (Θ_1) as

$$d\Theta = -dA/\Delta A \qquad (2)$$

In eq 2, A is the time-dependent absorbance at 526 nm and $\Delta A = A_1 - A_2$, where A_1 and A_2 are SPR absorbance values corresponding to fractional surface coverage by **1**, Θ_1, of 1 and 0, respectively.

To determine the dependence of rate on [**11-MU**], the concentration of **1** was set at 2.0 mM before mixing, corresponding to >97% coverage,[36] while concentrations of **11-MU** were varied from 8.0 to 32 μM. To determine the dependence of rate on [**1**], a single solution of **1**-protected Au NPs was used in the first syringe (2.0 mM **1** before mixing), while the second syringe contained 16.0 μM **11-MU** and variable concentrations of **1**, ranging from 0 to 6.0 mM. Each experimental run was repeated >20 times. After discarding small numbers (if any) of obviously erroneous traces, the remaining traces were averaged. The averaged trace was smoothed by the polynomial equation $y = \sum_{n=0}^{n=15} a_n x^n$ using Qtiplot software, and from the first derivative of the fitted curve, the rate maximum of the rapid-growth phase was calculated (see Results and Discussion section). The uncertainty in reaction-rate values, based on the signal-to-noise ratio of the traces, was estimated to be ±0.004 au s^{-1}. From the second derivative of the fitted curve, the durations of the slow phases were also measured, and uncertainties were estimated to be ±0.4 s based on repetitive kinetic runs. The relative absorbance drop over the slow phase (from statistical analysis of data obtained from all kinetic runs) was 5.5 ± 2.2% of ΔA (from eq 2). This value was used in calculations of nucleation rates and numbers of nucleation sites.

Acknowledgment. I.W. and F.S. thank the United States–Israel Binational Science Foundation (2008277), and I.W. thanks the Israel Science Foundation (248/09), for support. Y.W. thanks the Israeli Ministry of Education for a VATAT Post-Doctoral Fellowship.

Supporting Information Available: UV–vis spectra and titration data, additional cryo-TEM images, discussion, kinetic data, and analysis. This material is available free of charge *via* the Internet at http://pubs.acs.org.

REFERENCES AND NOTES

1. Love, J. C.; Estroff, L. A.; Kriebel, J. K.; Nuzzo, R. G.; Whitesides, G. M. Self-Assembled Monolayers of Thiolates on Metals

as a Form of Nanotechnology. *Chem. Rev.* **2005**, *105*, 1103–1170.
2. Stranick, S. J.; Parikh, A. N.; Tao, Y. T.; Allara, D. L.; Weiss, P. S. Phase Separation of Mixed-Composition Self-Assembled Monolayers into Nanometer Scale Molecular Domains. *J. Phys. Chem.* **1994**, *98*, 7636–7646.
3. Poirier, G. E.; Pylant, E. D. The Self-Assembly Mechanism of Alkanethiols on Au(111). *Science* **1996**, *272*, 1145–1148.
4. Bain, C. D.; Troughton, E. B.; Tao, Y. T.; Evall, J.; Whitesides, G. M.; Nuzzo, R. G. Formation of Monolayer Films by the Spontaneous Assembly of Organic Thiols from Solution onto Gold. *J. Am. Chem. Soc.* **1989**, *111*, 321–335.
5. Yamada, R.; Uosaki, K. *In Situ*, Real Time Monitoring of the Self-Assembly Process of Decanethiol on Au(111) in Liquid Phase. A Scanning Tunneling Microscopy Investigation. *Langmuir* **1997**, *13*, 5218–5221.
6. Tamada, K.; Hara, M.; Sasabe, H.; Knoll, W. Surface Phase Behavior of n-Alkanethiol Self-Assembled Monolayers Adsorbed on Au(111): An Atomic Force Microscope Study. *Langmuir* **1997**, *13*, 1558–1566.
7. Overney, R. M.; Meyer, E.; Frommer, J.; Brodbeck, D.; Luthi, R.; Howald, L.; Giintherodt, H. J.; Fujihira, M.; Takano, H.; Gotoh, Y. Friction Measurements on Phase-Separated Thin Films with a Modified Atomic Force Microscope. *Nature* **1992**, *359*, 133–135.
8. Doudevski, I.; Schwartz, D. K. Concentration Dependence of Self-Assembled Monolayer Island Nucleation and Growth. *J. Am. Chem. Soc.* **2001**, *123*, 6867–6872.
9. Murray, R. W. Nanoelectrochemistry: Metal Nanoparticles, Nanoelectrodes, and Nanopores. *Chem. Rev.* **2008**, *108*, 2688–2720.
10. Dahl, J. A.; Maddux, B. L. S.; Hutchison, J. E. Toward Greener Nanosynthesis. *Chem. Rev.* **2007**, *107*, 2228–2269.
11. Rooth, M.; Shaw, A. M. pH-Controlled Formation Kinetics of Self-Assembled Layers of Thioctic Acid on Gold Nanoparticles. *J. Phys. Chem. C* **2007**, *111*, 15363–15369.
12. Sardar, R.; Funston, A. M.; Mulvaney, P.; Murray, R. W. Gold Nanoparticles: Past, Present, and Future. *Langmuir* **2009**, *25*, 13840–13851.
13. Badia, A.; Demers, L.; Dickinson, L.; Morin, F. G.; Lennox, R. B.; Reven, L. Gold−Sulfur Interactions in Alkylthiol Self-Assembled Monolayers Formed on Gold Nanoparticles Studied by Solid-State NMR. *J. Am. Chem. Soc.* **1997**, *119*, 11104–11105.
14. Daniel, M.-C.; Astruc, D. Gold Nanoparticles: Assembly, Supramolecular Chemistry, Quantum-Size-Related Properties, and Applications toward Biology, Catalysis, and Nanotechnology. *Chem. Rev.* **2004**, *104*, 293–346.
15. Caragheorgheopol, A.; Chechik, V. Mechanistic Aspects of Ligand Exchange in Au Nanoparticles. *Phys. Chem. Chem. Phys.* **2008**, *10*, 5029–5041.
16. Jain, P. K.; Huang, X.; El-Sayed, I. H.; El-Sayed, M. A. Noble Metals on the Nanoscale: Optical and Photothermal Properties and Some Applications in Imaging, Sensing, Biology, and Medicine. *Acc. Chem. Res.* **2008**, *41*, 1578–1586.
17. Bardhan, R.; Lal, S.; Joshi, A.; Halas, N. J. Theranostic Nanoshells: From Probe Design to Imaging and Treatment of Cancer. *Acc. Chem. Res.* **2011**, *44*, 936–946.
18. Boisselier, E.; Astruc, D. Gold Nanoparticles in Nanomedicine: Preparations, Imaging, Diagnostics, Therapies and Toxicity. *Chem. Soc. Rev.* **2009**, *38*, 1759–1782.
19. Stewart, M. E.; Anderton, C. R.; Thompson, L. B.; Maria, J.; Gray, S. K.; Rogers, J. A.; Nuzzo, R. G. Nanostructured Plasmonic Sensors. *Chem. Rev.* **2008**, *108*, 494–521.
20. Corma, A.; Garcia, H. Supported Gold Nanoparticles as Catalysts for Organic Reactions. *Chem. Soc. Rev.* **2008**, *37*, 2096–2126.
21. Turner, M.; Golovko, V. B.; Vaughan, O. P. H; Abdulkin, P.; Berenguer-Murcia, A.; Tikhov, M. S.; Johnson, B. F. G.; Lambert, R. M. Selective Oxidation with Dioxygen by Gold Nanoparticle Catalysts Derived from 55-Atom Clusters. *Nature* **2008**, *454*, 981–983.
22. Hashmi, A. S. K.; Hutchings, G. J. Gold Catalysis. *Angew. Chem., Int. Ed.* **2006**, *45*, 7896–7936.
23. Hughes, M. D.; Xu, Y.-J.; Jenkins, P.; McMorn, P.; Landon, P.; Enache, D. I.; Carley, A. F.; Attard, G. A.; Hutchings, G. J.; King, F.; *et al*. Tunable Gold Catalysts for Selective Hydrocarbon Oxidation under Mild Conditions. *Nature* **2005**, *437*, 1132–1135.
24. Liu, K.; Nie, Z.; Zhao, N.; Li, W.; Rubinstein, M.; Kumacheva, E. Step-Growth Polymerization of Inorganic Nanoparticles. *Science* **2010**, *329*, 197–200.
25. Prasad, B. L. V.; Sorensen, C. M.; Klabunde, K. J. Gold Nanoparticle Superlattices. *Chem. Soc. Rev.* **2008**, *37*, 1871–1883.
26. Stellacci, F. Nanoscale Materials—a New Season. *Nat. Mater.* **2005**, *4*, 113–114.
27. Zhang; Glotzer, S. C. Self-Assembly of Patchy Particles. *Nano Lett.* **2004**, *4*, 1407–1413.
28. Kairdolf, B. A.; Nie, S. Multidentate-Protected Colloidal Gold Nanocrystals: pH Control of Cooperative Precipitation and Surface Layer Shedding. *J. Am. Chem. Soc.* **2011**, *133*, 7268–7271.
29. Ha, J.-M.; Solovyov, A.; Katz, A. Postsynthetic Modification of Gold Nanoparticles with Calix[4]arene Enantiomers: Origin of Chiral Surface Plasmon Resonance. *Langmuir* **2008**, *25*, 153–158.
30. Weisbecker, C. S.; Merritt, M. V.; Whitesides, G. M. Molecular Self-Assembly of Aliphatic Thiols on Gold Colloids. *Langmuir* **1996**, *12*, 3763–3772.
31. Centrone, A.; Penzo, E.; Sharma, M.; Myerson, J. W.; Jackson, A. M.; Marzari, N.; Stellacci, F. The Role of Nanostructure in the Wetting Behavior of Mixed-Monolayer-Protected Metal Nanoparticles. *Proc. Natl. Acad. Sci. U. S. A.* **2008**, *105*, 9886–9891.
32. DeVries, G. A.; Brunnbauer, M.; Hu, Y.; Jackson, A. M.; Long, B.; Neltner, B. T.; Uzun, O.; Wunsch, B. H.; Stellacci, F. Divalent Metal Nanoparticles. *Science* **2007**, *315*, 358–361.
33. Jackson, A. M.; Myerson, J. W.; Stellacci, F. Spontaneous Assembly of Subnanometre-Ordered Domains in the Ligand Shell of Monolayer-Protected Nanoparticles. *Nat. Mater.* **2004**, *3*, 330–336.
34. Bellino, M. G.; Calvo, E. J.; Gordillo, G. Adsorption Kinetics of Charged Thiols on Gold Nanoparticles. *Phys. Chem. Chem. Phys.* **2004**, *6*, 424–428.
35. Neyman, A.; Meshi, L.; Zeiri, L.; Weinstock, I. A. Direct Imaging of the Ligand Monolayer on an Anion-Protected Metal Nanoparticle through Cryogenic Trapping of its Solution-State Structure. *J. Am. Chem. Soc.* **2008**, *130*, 16480–16481.
36. Wang, Y. F.; Neyman, A.; Arkhangelsky, E.; Gitis, V.; Meshi, L.; Weinstock, I. A. Self-Assembly and Structure of Directly Imaged Inorganic-Anion Monolayers on a Gold Nanoparticle. *J. Am. Chem. Soc.* **2009**, *131*, 17412–17422.
37. Weinstock, I. A.; Müller, A. Special Issue: Frontiers in Metal Oxide Cluster Science. *Isr. J. Chem* **2011**, *51*, 169–302.
38. Long, D.-L.; Tsunashima, R.; Cronin, L. Polyoxometalates: Building Blocks for Functional Nanoscale Systems. *Angew. Chem., Int. Ed.* **2010**, *49*, 1736–1758.
39. Pope, M. T. From Biology to Nanotechnology. In *Comprehensive Coordination Chemistry II: From Biology to Nanotechnology*; Wedd, A. G., Eds.; Elsevier: Oxford, 2004; pp 635−678.
40. Cowan, J. J.; Hill, C. L.; Reiner, R. S.; Weinstock, I. A. Dodecatungstoaluminic Acid and its Monolacunary and Mixed-Addendum Derivatives. In *Inorganic Syntheses*; Coucouvanis, D., Eds.; John Wiley & Sons, Inc.: New York, 2002; pp 18−26.
41. Cowan, J. J.; Bailey, A. J.; Heintz, R. A.; Do, B. T.; Hardcastle, K. I.; Hill, C. L.; Weinstock, I. A. Formation, Isomerization, and Derivatization of Keggin Tungstoaluminates. *Inorg. Chem.* **2001**, *40*, 6666–6675.
42. Weinstock, I. A.; Cowan, J. J.; Barbuzzi, E. M. G.; Zeng, H. D.; Hill, C. L. Equilibria between α and β Isomers of Keggin Heteropolytungstates. *J. Am. Chem. Soc.* **1999**, *121*, 4608–4617.
43. Wang, Y.; Zeiri, O.; Gitis, V.; Neyman, A.; Weinstock, I. A. Reversible Binding of an Inorganic Cluster-Anion to the Surface of a Gold Nanoparticle. *Inorg. Chim. Acta* **2010**, *363*, 4416–4420.

44. Kirk, J. S.; Bohn, P. W. Surface Adsorption and Transfer of Organomercaptans to Colloidal Gold and Direct Identification by Matrix Assisted Laser Desorption/Ionization Mass Spectrometry. *J. Am. Chem. Soc.* **2004**, *126*, 5920–5926.
45. Schessler, H. M.; Karpovich, D. S.; Blanchard, G. J. Quantitating the Balance between Enthalpic and Entropic Forces in Alkanethiol/Gold Monolayer Self Assembly. *J. Am. Chem. Soc.* **1996**, *118*, 9645–9651.
46. Jiménez, A.; Sarsa, A.; Blázquez, M.; Pineda, T. A Molecular Dynamics Study of the Surfactant Surface Density of Alkanethiol Self-Assembled Monolayers on Gold Nanoparticles as a Function of the Radius. *J. Phys. Chem. C* **2010**, *114*, 21309–21314.
47. Heaven, M. W.; Dass, A.; White, P. S.; Holt, K. M.; Murray, R. W. Crystal Structure of the Gold Nanoparticle $[N(C_8H_{17})_4][Au_{25}(SCH_2CH_2Ph)_{18}]$. *J. Am. Chem. Soc.* **2008**, *130*, 3754–3755.
48. Jadzinsky, P. D.; Calero, G.; Ackerson, C. J.; Bushnell, D. A.; Kornberg, R. D. Structure of a Thiol Monolayer-Protected Gold Nanoparticle at 1.1 Å Resolution. *Science* **2007**, *318*, 430–433.
49. Cossaro, A.; Mazzarello, R.; Rousseau, R.; Casalis, L.; Verdini, A.; Kohlmeyer, A.; Floreano, L.; Scandolo, S.; Morgante, A.; Klein, M. L.; *et al*. X-ray Diffraction and Computation Yield the Structure of Alkanethiols on Gold(111). *Science* **2008**, *321*, 943–946.
50. Hostetler, M. J.; Wingate, J. E.; Zhong, C.-J.; Harris, J. E.; Vachet, R. W.; Clark, M. R.; Londono, J. D.; Green, S. J.; Stokes, J. J.; Wignall, G. D.; *et al*. Alkanethiolate Gold Cluster Molecules with Core Diameters from 1.5 to 5.2 nm: Core and Monolayer Properties as a Function of Core Size. *Langmuir* **1998**, *14*, 17–30.
51. Terrill, R. H.; Postlethwaite, T. A.; Chen, C.-h.; Poon, C.-D.; Terzis, A.; Chen, A.; Hutchison, J. E.; Clark, M. R.; Wignall, G. Monolayers in Three Dimensions: NMR, SAXS, Thermal, and Electron Hopping Studies of Alkanethiol Stabilized Gold Clusters. *J. Am. Chem. Soc.* **1995**, *117*, 12537–12548.
52. Jackson, A. M.; Hu, Y.; Silva, P. J.; Stellacci, F. From Homoligand- to Mixed-Ligand- Monolayer-Protected Metal Nanoparticles: A Scanning Tunneling Microscopy Investigation. *J. Am. Chem. Soc.* **2006**, *128*, 11135–11149.
53. Viudez, A. J.; Madueño,, R.; Blázquez, M.; Pineda, T. Synthesis, Characterization, and Double Layer Capacitance Charging of Nanoclusters Protected by 6-Mercaptopurine. *J. Phys. Chem. C* **2009**, *113*, 5186–5192.
54. Kakiuchi, T.; Iida, M.; Gon, N.; Hobara, D.; Imabayashi, S.-I.; Niki, K. Miscibility of Adsorbed 1-Undecanethiol and 11-Mercaptoundecanoic Acid Species in Binary Self-Assembled Monolayers on Au(111). *Langmuir* **2001**, *17*, 1599–1603.
55. Vilain, C.; Goettmann, F.; Moores, A.; Le Floch, P.; Sanchez, C. Study of Metal Nanoparticles Stabilised by Mixed Ligand Shell: a Striking Blue Shift of the Surface-Plasmon Band Evidencing the Formation of Janus Nanoparticles. *J. Mater. Chem.* **2007**, *17*, 3509–3514.
56. Singh, C.; Ghorai, P. K.; Horsch, M. A.; Jackson, A. M.; Larson, R. G.; Stellacci, F.; Glotzer, S. C. Entropy-Mediated Patterning of Surfactant-Coated Nanoparticles and Surfaces. *Phys. Rev. Lett.* **2007**, *99*, 226106.
57. Saavedra, H. M.; Barbu, C. M.; Dameron, A. A.; Mullen, T. J.; Crespi, V. H.; Weiss, P. S. 1-Adamantanethiolate Monolayer Displacement Kinetics Follow a Universal Form. *J. Am. Chem. Soc.* **2007**, *129*, 10741–10746.
58. Fotsing, E. R. Phase Transformation Kinetics and Microstructure of Carbide and Diboride Based Ceramics. Doctoral Thesis, Technische Universität Clausthal, Germany, 2005.
59. Ruitenberg, G.; Petford-Long, A. K.; Doole, R. C. Determination of the Isothermal Nucleation and Growth Parameters for the Crystallization of Thin $Ge_2Sb_2Te_5$ Flms. *J. Appl. Phys.* **2002**, *92*, 63116–3123.
60. Wang, Y.; Weinstock, I. A. Cation Mediated Self-Assembly of Inorganic Cluster Anion Building Blocks. *Dalton Trans.* **2010**, *39*, 6143–6152.
61. Song, Y.; Murray, R. W. Dynamics and Extent of Ligand Exchange Depend on Electronic Charge of Metal Nanoparticles. *J. Am. Chem. Soc.* **2002**, *124*, 7096–7102.
62. Kimling, J.; Maier, M.; Okenve, B.; Kotaidis, V.; Ballot, H.; Plech, A. Turkevich Method for Gold Nanoparticle Synthesis Revisited. *J. Phys. Chem. B* **2006**, *110*, 15700–15707.
63. Wang, D.; Nap, R. J.; Lagzi, I.; Kowalczyk, B.; Han, S.; Grzybowski, B. A.; Szleifer, I. How and Why Nanoparticle's Curvature Regulates the Apparent pK_a of the Coating Ligands. *J. Am. Chem. Soc.* **2011**, *133*, 2192–2197.